

Role of antisite disorder, electron-electron correlations, and a surface valence transition in the electronic structure of CeMnNi₄

Pampa Sadhukhan,¹ Sunil Wilfred D'Souza,^{1,*} Vipin Kumar Singh,¹ Rajendra Singh Dhaka,^{1,†} Andrei Gloskovskii,² Sudesh Kumar Dhar,³ Pratap Raychaudhuri,³ Ashish Chainani,⁴ Aparna Chakrabarti,^{5,6} and Sudipta Roy Barman¹

¹UGC-DAE Consortium for Scientific Research, Khandwa Road, Indore 452001, Madhya Pradesh, India

²Deutsches Elektronen-Synchrotron DESY, Notkestrasse 85, D-22607 Hamburg, Germany

³Department of Condensed Matter Physics and Materials Science, Tata Institute of Fundamental Research, Homi Bhabha Road, Colaba, Mumbai 400005, India

⁴National Synchrotron Radiation Research Center, Hsinchu 30076, Taiwan

⁵Theory and Simulations Laboratory, Raja Ramanna Centre for Advanced Technology, Indore, 452013, India

⁶Homi Bhabha National Institute, Anushakti Nagar, Mumbai, 400094, India



(Received 2 June 2018; revised manuscript received 13 November 2018; published 2 January 2019)

CeMnNi₄ exhibits an unusually large spin polarization, but its origin has baffled researchers for more than a decade. We use bulk sensitive hard x-ray photoelectron spectroscopy (HAXPES) and density functional theory based on the Green's function technique to demonstrate the importance of electron-electron correlations of both the Ni 3*d* (U_{Ni}) and Mn 3*d* (U_{Mn}) electrons in explaining the valence band of this multiply correlated material. We show that Mn-Ni antisite disorder as well as U_{Ni} play a crucial role in enhancing its spin polarization: Antisite disorder broadens a Ni 3*d* minority-spin peak close to the Fermi level (E_F), while an increase in U_{Ni} shifts it toward E_F , both leading to a significant increase of minority-spin states at E_F . Furthermore, the rare occurrence of a valence state transition between the bulk and the surface is demonstrated highlighting the importance of HAXPES in resolving the electronic structure of materials unhindered by surface effects.

DOI: [10.1103/PhysRevB.99.035102](https://doi.org/10.1103/PhysRevB.99.035102)

I. INTRODUCTION

In recent years, hard x-ray photoelectron spectroscopy (HAXPES) has turned out to be a reliable tool to study the electronic structure of correlated systems, thin films, and buried interfaces of materials, thus providing new insights into their physical properties [1–3]. In this paper, we present the first study of the electronic structure of CeMnNi₄, an interesting material with large spin transport polarization of 66% [4], using HAXPES and density functional theory (DFT) calculations based on the spin-polarized relativistic Korringa-Kohn-Rostoker (SPRKKR) method [5]. CeMnNi₄ has a cubic MgCu₄Sn-type structure [6]; it is ferromagnetic with a magnetic moment of 4.95 μ_B and Curie temperature of 140 K [4]. These encouraging properties of CeMnNi₄ started a flurry of activity aimed at understanding its electronic structure [7–9]. However, no photoemission study of its electronic structure has been reported to date, and the theoretical studies so far have been unable to explain the different aspects of its electronic structure and its spin polarization in particular. The early DFT calculations [7] reported a spin polarization [10] (P_0) value of about 16–20%; and the much larger experimental polarization was attributed to disorder or

nonstoichiometry of the specimens. In fact, in a subsequent x-ray absorption fine structure (XAFS) study, about 6% Mn-Ni antisite disorder was reported [8]. The authors also performed a DFT calculation using the pseudopotential method as implemented in the VASP code, including an ordered antisite defect configuration of nearest-neighbor Ni and Mn that were site exchanged. Thus, in this approach, the effect of randomly disordered antisite defects is not taken into account. Their results, however, showed a significant increase in P_0 , which was not related to disorder, but rather to enhanced minority spin states of the site-exchanged Mn 3*d* partial density of states (PDOS) due to hybridization with neighboring Ni atom [8]. On the other hand, another DFT calculation that considered electron-electron correlation of the Mn 3*d* electrons (U_{Mn}) but no antisite defect showed that P_0 increases with U_{Mn} [9]. In the absence of any photoemission study and its direct comparison with theory that addresses the influence of both antisite disorder and correlation, their role in determining the electronic structure and spin polarization of CeMnNi₄ has remained an unresolved question until date.

In this paper, we show that both antisite disorder and electron-electron correlations for Ni 3*d* (U_{Ni}) and Mn 3*d* (U_{Mn}) electrons have a crucial influence on the bulk electronic structure of CeMnNi₄. In addition, since U_{Ce} is typically taken to be about 7 eV in Ce intermetallics [11], CeMnNi₄ can be regarded as a multiply correlated system, further complicated by the presence of inherent disorder [8]. U_{Ni} and U_{Mn} are responsible for determining the energy positions of the peaks in the valence band (VB) and their optimum values

*Present address: New Technologies Research Centre, University of West Bohemia, Univerzitní 8, CZ-306 14 Pilsen, Czech Republic.

†Present address: Department of Physics, Indian Institute of Technology Delhi, Hauz Khas, New Delhi 110016, India.

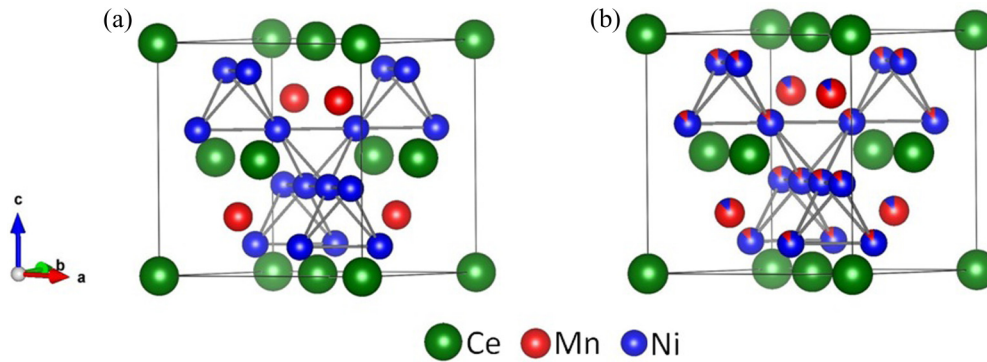


FIG. 1. The crystal structure of (a) ordered CeMnNi_4 with Ce and Mn placed at $4a$ (0, 0, 0) and $4c$ (0.25, 0.25, 0.25) sites, respectively, while Ni is placed at $16e$ (0.624, 0.624, 0.624) site. The corresponding multiplicities of $4a$, $4c$, and $16e$ atomic sites are 1, 1, and 4, respectively, and (b) disordered CeMnNi_4 with 12% ($x = 0.12$) Mn-Ni antisite disorder. The crystallographic axes are represented by the arrows (a , b , c). The entire cubic structure has been rotated by 45° in the clockwise direction to provide a better view. Note that the first nearest neighbor (nn) of Mn_{Mn} (Mn atom in Mn position) is three Ni atoms, while the second nn is four Ce atoms. On the other hand, for Mn_{Ni} (Mn atom in Ni position), the first nn is six Ni atoms, while the second nn is three Mn_{Mn} atoms.

($U_{\text{Mn}} = 4.5$ eV, $U_{\text{Ni}} = 6.5$ eV) are obtained by the best agreement between theoretically calculated and experimental HAXPES VBs. A surprising result is that the large P_0 of CeMnNi_4 has two origins: the antisite disorder (x) and U_{Ni} . The former broadens a minority spin Ni $3d$ peak close to E_F , while the latter shifts it toward E_F . Thus, in both cases, the minority spin total DOS at E_F ($n_\downarrow(E_F)$) increases, while the majority spin total DOS ($n_\uparrow(E_F)$) remains essentially unchanged, resulting in a clear enhancement of P_0 . The total magnetic moment exhibits contrasting variation: a decrease with x and an increase with U_{Ni} . Furthermore, rare occurrence of a valence state transition on the surface of a ternary material is demonstrated: a bulk mixed valent state transforms to a nearly trivalent Ce^{3+} state due to the weakened hybridization on the surface. This highlights the importance of HAXPES in resolving the electronic structure of materials unhindered by surface effects.

II. EXPERIMENTAL AND COMPUTATIONAL METHODS

HAXPES measurements were performed at the P09 beamline in PETRA III synchrotron center, Germany, on polycrystalline CeMnNi_4 ingot that was cleaved under ultrahigh vacuum at 2×10^{-8} mbar pressure to expose a fresh surface. The spectra were recorded by using a Phoibos 225 analyzer with 30 eV pass energy at 50 K [12]. Photons were incident on the sample at a grazing angle (10°) and the photoelectrons were collected in the nearly normal emission geometry. The total instrumental resolution (including both source and analyzer contributions), obtained from the least-squares fitting of the Au Fermi edge in electrical contact with the specimen is 0.26 eV. The stoichiometric ingot of CeMnNi_4 was prepared by an arc melting method and characterized for its structure using x-ray diffraction, as discussed in Ref. [4].

The bulk ground-state properties of CeMnNi_4 have been calculated in $F43m$ symmetry using the experimental lattice parameter ($a = 6.9706$ Å) as determined by neutron powder diffraction at 17 K [6]. Disordered Mn-Ni antisite defects have been considered by setting the $16e$ site occupations to $1-0.25x$ for Ni_{Ni} and $0.25x$ for Mn_{Ni} , while the occupancies at the $4c$

site were set to $1-x$ for Mn_{Mn} and x for Ni_{Mn} , where X_Z refers to an X atom at a Z atom site ($X, Z = \text{Ni}, \text{Mn}$). Here, x quantifies the amount of antisite disorder as the fraction of Mn atoms occupying the Ni sites. In this paper, we have varied x from 0 to 0.12 and the crystal structures are shown in Fig. 1.

Self-consistent band-structure calculations were carried out using fully relativistic SPRKKR method in the atomic sphere approximation [5]. The exchange and correlation effects were incorporated within the generalized gradient approximation framework [13]. The electron-electron correlation has been taken into account as described in the LSDA+U scheme [14]. The parameters of screened on-site Coulomb interaction U for all the components (U_{Ni} , U_{Mn} , and U_{Ce}) have been varied up to 7 eV, with the exchange interaction J fixed at 0.8 eV. The static double counting of LSDA+U approach has been corrected using the atomic limit scheme. The angular momentum expansion up to $l_{\text{max}} = 4$ has been used for each atom. The energy convergence criterion and coherent potential approximation tolerance has been set to 10^{-5} Ry. Brillouin zone integrations were performed on a $36 \times 36 \times 36$ mesh of k -points in the irreducible wedge of the Brillouin zone. We have employed Lloyd's formula, which provides an accurate determination of the Fermi level and density of states [15]. For calculating the angle-integrated VB spectrum, all the PDOS contributions from s , p , d , and f states of Ce, Mn, and Ni were multiplied with the corresponding photoemission cross-sections and then added [16,17]. This is multiplied by the Fermi function and convoluted with the instrumental resolution and an energy-dependent lifetime broadening $0.04 \times (E_B - E_F)$ [18]. Furthermore, to simulate the inelastic background, both Shirley background [19] and an asymmetric background suggested for HAXPES have been used [20].

The Ce $3d$ core-level spectra were fitted using a least-squares error minimization routine with each peak assigned a Doniach and Šunjić (DS) line shape [21]. This was further convoluted with a Gaussian function of fixed width to represent the instrumental broadening, 0.26 eV and 1.2 eV for HAXPES and XPS, respectively. Since Ni $2p$ that appears close in binding energy to Ce $3d$ might contribute to the

intensity in the Ce $3d$ region, the Ni $2p$ peaks were also included in the fitting scheme. The whole region including Ni $2p$ along with the components is shown in Fig. S1 of the Supplemental Material [22]. A total of ten DS line shapes were used: six for Ce $3d$ comprising the three f^n components for each spin-orbit (s.o.) peak and four for Ni $2p$ representing the main peak and satellite for both s.o. components. The parameters defining each DS line shape are the intensity, position, width (Γ), and asymmetry parameter (α). An inelastic background was also included in the fitting scheme [20]. Thus, a total of 35 parameters defined the full spectral shape, including Ce $3d$ and Ni $2p$. However, some reasonable constraints were needed; for example, (i) the lifetime broadening of f^0 for Ce $3d_{3/2}$ was constrained to be greater than or equal to f^0 for Ce $3d_{5/2}$, (ii) α was kept equal for all Ce $3d$ DS components, and (iii) for XPS fitting, the satellites of Ni $2p$ have same width as HAXPES.

A. Valence band of CeMnNi₄

The HAXPES VB spectrum recorded with 8 keV photon energy at 50 K shows a step (S) close to E_F at -0.4 eV; peaks at -1.5 (A), -2.2 (B), -3.6 (C), -4.2 (D), -5.2 eV (E), and a weak shoulder at -6 eV (F) [Fig. 2(a)]. To ascertain their origin and study the influence of disorder on the spectral shape, we have calculated the VB spectra in Fig. 2(a) without (red line with open circles, $x = 0$) and with 6% Mn-Ni antisite disorder (blue dashed line, $x = 0.06$). The VB spectra are calculated from the partial DOS (PDOS) shown in Fig. 3. Six-percent disorder is considered because a previous XAFS study [8] inferred a disorder of this magnitude on a specimen that was prepared by the same procedure as ours. We find that disorder results in a small but finite broadening of the VB, but it has no effect on the position of the peaks. However, comparison of the calculated HAXPES VB with experiment shows glaring differences: the peaks corresponding to A and B (black arrows) are positioned at higher and lower energies, respectively, and thus their separation (1.6 eV) is significantly larger compared to experiment (0.7 eV). The peak at -5.4 eV (red arrow) is shifted with respect to peak E of the experimental VB, the peak at -3.3 eV (red tick) appears at a dip, while there is no peak in the theory corresponding to F (see the blue dashed arrows). In Fig. 3, DOS calculated with disorder up to $x = 0.12$ i.e., 12% antisite disorder) shows increased broadening, but the positions of all the peaks remain unchanged.

Thus, it is obvious from the above discussion that disorder is unable to explain the experimental VB. So, we examine the possible role of correlation starting with U_{Mn} . As U_{Mn} is increased, interesting modifications in the -3 to -6 eV region are observed in Fig. 2(a), which are primarily related to the systematic changes in the Mn $3d$ contribution to the VB [Fig. 2(b), which is calculated from the Mn $3d$ PDOS shown in Fig. 4]. At $U_{Mn} = 0$, the Mn $3d$ states are delocalized over 0 to -5 eV with the most intense peak at -3.3 eV. Increase of U_{Mn} narrows the Mn $3d$ PDOS, the peak intensity increases and it shifts by a large amount to lower energies, i.e., away from E_F e.g., -5.2 eV for $U_{Mn} = 4.5$ eV). The best agreement with experiment in the -3 to -6 eV region is obtained for $U_{Mn} = 4.5$ eV (black line), where the peaks at -3.6 , -4.2 ,

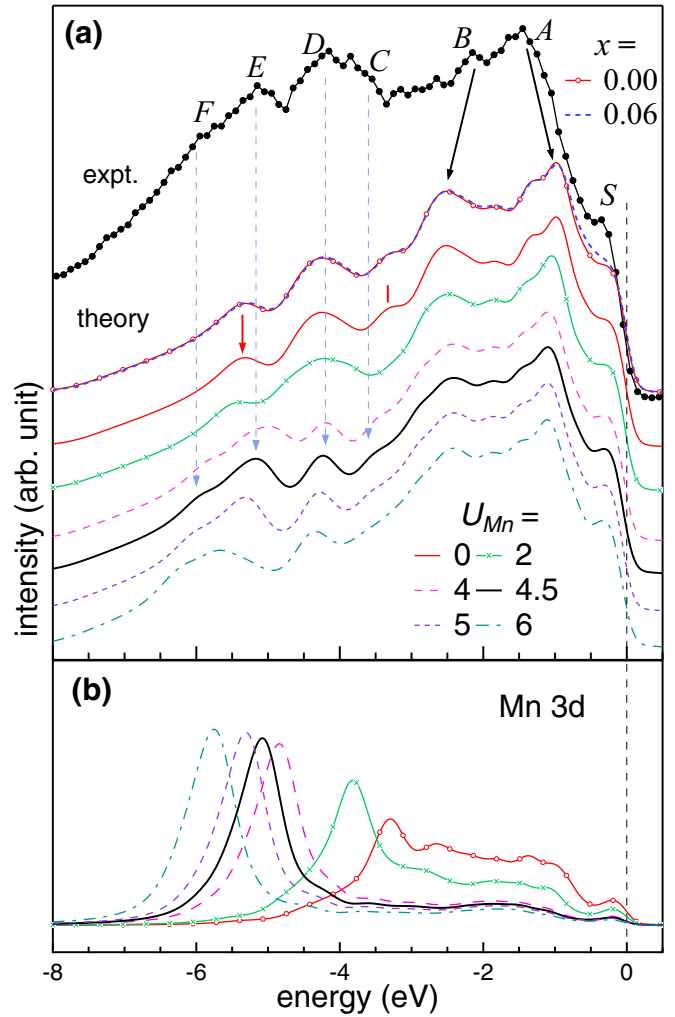


FIG. 2. (a) The valence band (VB) HAXPES spectra of CeMnNi₄ at 50 K using 8 keV photon energy (black filled circles) compared with the calculated VB spectra for $x = 0$ (no disorder) and $x = 0.06$ (6% Mn-Ni antisite disorder). The VBs calculated with different U_{Mn} are shown, where $x = 0$, $U_{Ni} = U_{Ce} = 0$ eV. The zero of the horizontal energy scale corresponds to the Fermi level (E_F). The spectra are staggered along the vertical axis for clarity of presentation, and the zero of the intensity for each spectrum is indicated by the constant spectral region above E_F (b) Mn $3d$ contribution to the calculated VB as a function of U_{Mn} .

-5.2 , and -6 eV appear at the same positions as C , D , E , and F , respectively, of the experimental VB, as shown by the blue dashed arrows in Fig. 2(a). The Mn $3d$ states contribute to the peak E along with Ni $4s$ states. However, its intensity is relatively less due to smaller photoemission cross section of Mn $3d$ with respect to Ni $3d$ at 8 keV [16].

Although $U_{Mn} = 4.5$ eV provides a good agreement for peaks C - F , the positions of the peaks A and B are not well reproduced as these remain unaltered with U_{Mn} (Fig. 4). It is evident that A and B originate primarily from Ni $3d$ states, and so we calculate the VB by introducing U_{Ni} , with U_{Mn} fixed at 4.5 eV. We find that as U_{Ni} increases, the peak at -2.6 eV shifts to higher energy, i.e., toward E_F (blue dashed line) and appears close to the position of peak B for

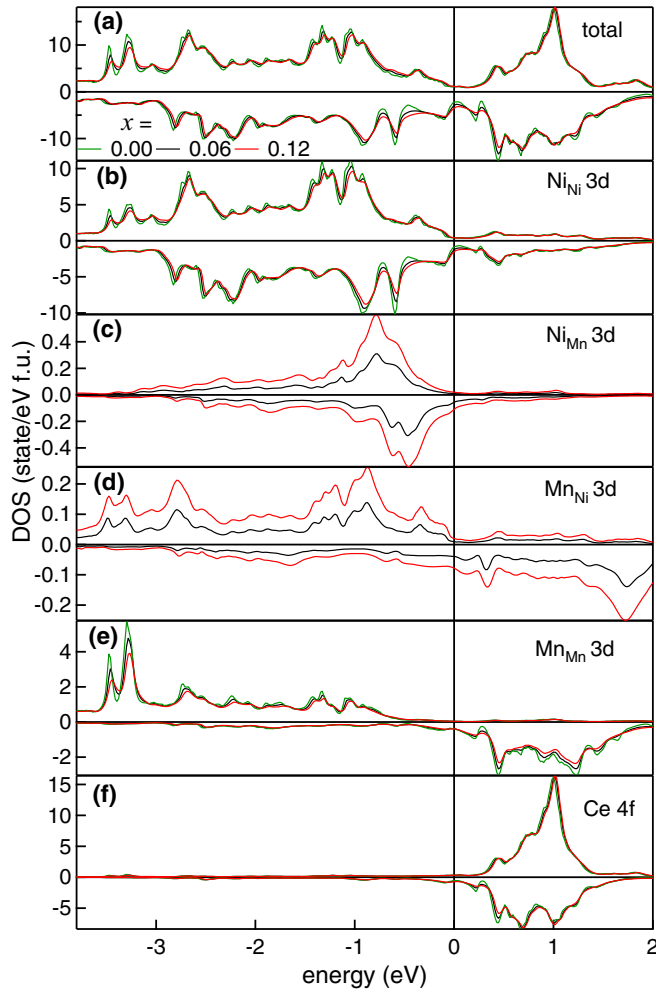


FIG. 3. Spin-polarized (a) total DOS and the PDOS for (b) $\text{Ni}_{\text{Ni}} 3d$, (c) $\text{Ni}_{\text{Mn}} 3d$, (d) $\text{Mn}_{\text{Ni}} 3d$, (e) $\text{Mn}_{\text{Mn}} 3d$, and (f) $\text{Ce } 4f$ as a function of Mn-Ni antisite disorder quantified by $x = 0, 0.06$ and 0.12 .

$U_{\text{Ni}} = 6.5$ eV (Fig. 5, see Fig. 6 for PDOS). On the other hand, the peak at -1.1 eV initially shifts to higher energies and eventually shifts back to lower energy (green dashed line) toward peak A. The separation of these two peaks is lowest (0.8 eV) at $U_{\text{Ni}} = 7$ eV. However, for $U_{\text{Ni}} = 7$ eV, a new peak appears at -0.7 eV in disagreement with experiment. Thus, we conclude that the best agreement is observed for $U_{\text{Ni}} = 6.5$ eV, where the positions as well as the separation (0.9 eV) of the calculated peaks agree well with A and B (black dashed arrows in Fig. 5). Note that the peaks in the -3 to -6 eV region in the total VB are hardly affected by U_{Ni} .

It is to be noted that in Fig. 5, we also consider a value of $U_{\text{Ce}} (=7$ eV) for the $\text{Ce } 4f$ electrons that is generally observed in Ce intermetallic compounds [11]. However, U_{Ce} does not have any discernible effect on the occupied states and the VB, since the $\text{Ce } 4f$ peak appears mostly above E_F at 0.9 eV for $U_{\text{Ce}} = 0$ [Fig. 4(c)] and shifts to higher energy (1.2 eV) for $U_{\text{Ce}} = 7$ eV [Fig. 6(a)]. Thus, due to the significant variation of Ni and Mn $3d$ states with U_{Ni} and U_{Mn} , respectively, and taking U_{Ce} from literature [11], we are able to determine the optimum values of U for CeMnNi_4 to be $U_{\text{Mn}} = 4.5$ eV, $U_{\text{Ni}} =$

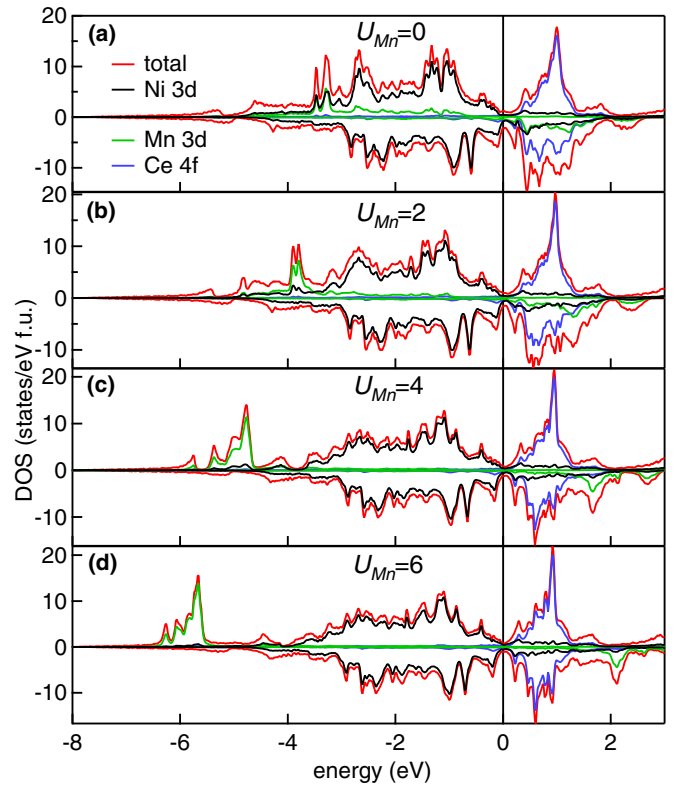


FIG. 4. Spin-polarized total DOS and Ni $3d$, Mn $3d$, and Ce $4f$ PDOS as a function of U_{Mn} with $U_{\text{Ni}} = U_{\text{Ce}} = 0$ and $x = 0$, where for (a) $U_{\text{Mn}} = 0$ eV, (b) $U_{\text{Mn}} = 2$ eV, (c) $U_{\text{Mn}} = 4$ eV, and (d) $U_{\text{Mn}} = 6$ eV.

6.5 eV and $U_{\text{Ce}} = 7$ eV (referred henceforth as $U(4.5, 6.5, 7)$). The partial contributions of the different PDOS to each of the peaks in the total VB for $U(4.5, 6.5, 7)$ as well as the effect

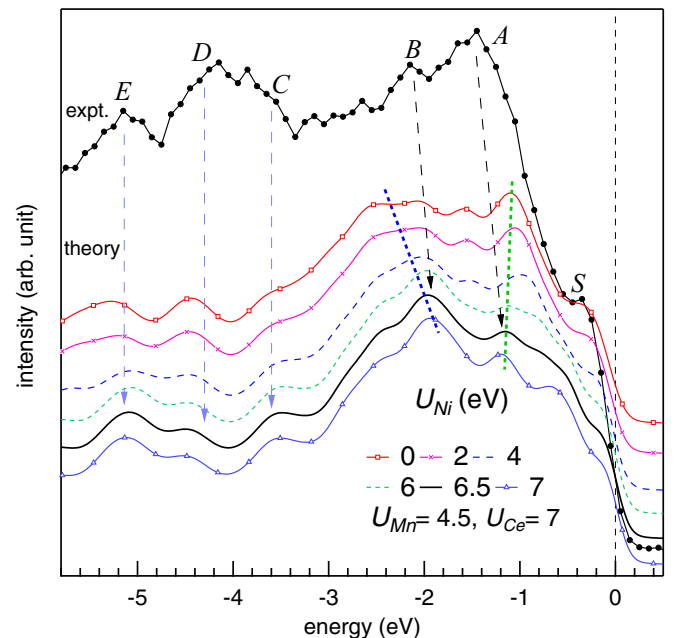


FIG. 5. The valence band HAXPES spectrum of Fig. 2 (black filled circles) compared with calculated VB spectra as a function of U_{Ni} , with $U_{\text{Mn}} = 4.5$ eV, $U_{\text{Ce}} = 7$ eV and $x = 0$.

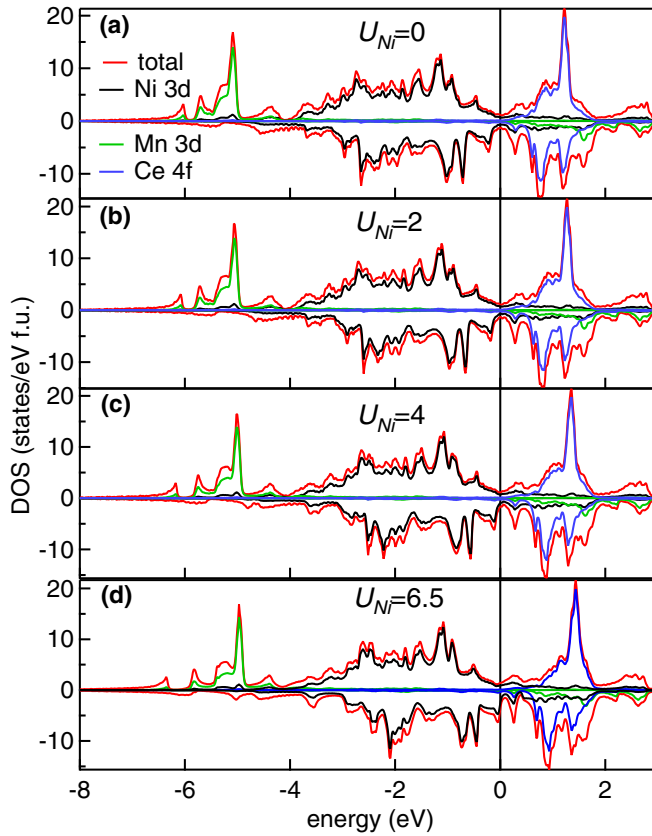


FIG. 6. Spin-polarized total DOS and Ni 3d, Mn 3d, and Ce 4f PDOS as a function of U_{Ni} with fixed $U_{\text{Mn}} = 4.5$ eV and $U_{\text{Ce}} = 7$ eV where for (a) $U_{\text{Ni}} = 0$ eV, (b) $U_{\text{Ni}} = 2$ eV, (c) $U_{\text{Ni}} = 4$ eV, and (d) $U_{\text{Ni}} = 6.5$ eV.

of the different inelastic backgrounds are shown in Fig. 7. Light-blue dashed lines show that the energy positions of the features in the calculated VB are independent of the shape of the background function. Features A, B, and S originate primarily from Ni 3d states, while B has some contribution from Ce 5d and Ni 4p. C and D are related primarily to Ni 4s with some contribution from Ce 5d and Mn 4s. Feature E is due to Mn 3d as well as Ni 4s and Mn 4s states, while F appears primarily due to Ni 4s states.

B. Spin polarization and magnetic moments

We find that the Mn-Ni antisite disorder has an unexpected positive effect on the spin polarization (P_0). As shown in Fig. 8(a) and Table I, P_0 exhibits a monotonic increase with x , reaching a value of 45% (50%) for $x = 0.06$ (0.12). This is an important result since in half metals and Heusler alloys, a low experimental value of P_0 is generally attributed to disorder [23]. To understand the reason for this unusual behavior, we show the spin-polarized total DOS around E_F in Fig. 8(b). A peak in the minority spin DOS close to E_F at -0.1 eV progressively broadens and also shifts by a small amount (≈ 15 meV) toward E_F resulting in increase of $n_{\downarrow}(E_F)$ with x . On the contrary, the structureless majority spin DOS and consequently $n_{\uparrow}(E_F)$ remain almost unchanged. Thus, this contrasting behavior of $n_{\downarrow}(E_F)$ and $n_{\uparrow}(E_F)$ brings about the

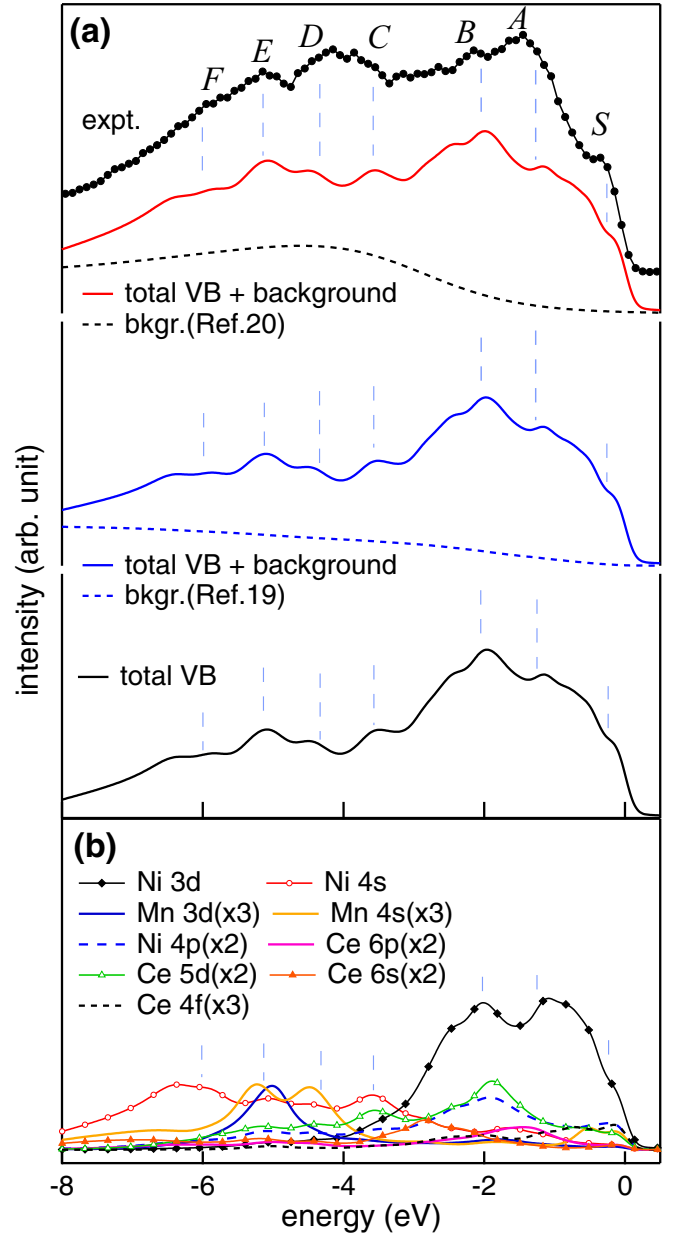


FIG. 7. (a) The calculated total valence band spectra for $U(4.5,6.5,7)$ with Tougaard [20] background (bkg.) (top), Shirley [19] background (middle), and no background (bottom) are compared with the experimental HAXPES VB spectrum. (b) The different partial contributions to the total VB. The light blue dashed lines indicate the positions of different features in the calculated VB.

increase of P_0 with x [Fig. 8(a)]. Table I defines and shows the partial contributions from Ni 3d ($P_{0\text{Ni}3d}$), Mn 3d ($P_{0\text{Mn}3d}$), and Ce 4f ($P_{0\text{Ce}4f}$) PDOS to P_0 for different x , and we find that P_0 increases solely because of $P_{0\text{Ni}3d}$. This is also confirmed in Fig. 9, where the peak in the minority spin DOS is clearly dominated by Ni 3d PDOS (black tick).

Turning to the influence of U on P_0 [Fig. 8(c)], we find that it increases with U_{Ni} from about 3.8% for $U(4.5,0,7)$ to 45% for $U_{\text{Ni}} = 6.5$ eV, i.e., for the optimum $U(4.5,6.5,7)$. This is related to increase of $n_{\downarrow}(E_F)$ due to a significant shift of the minority spin total DOS peak toward E_F from -0.2

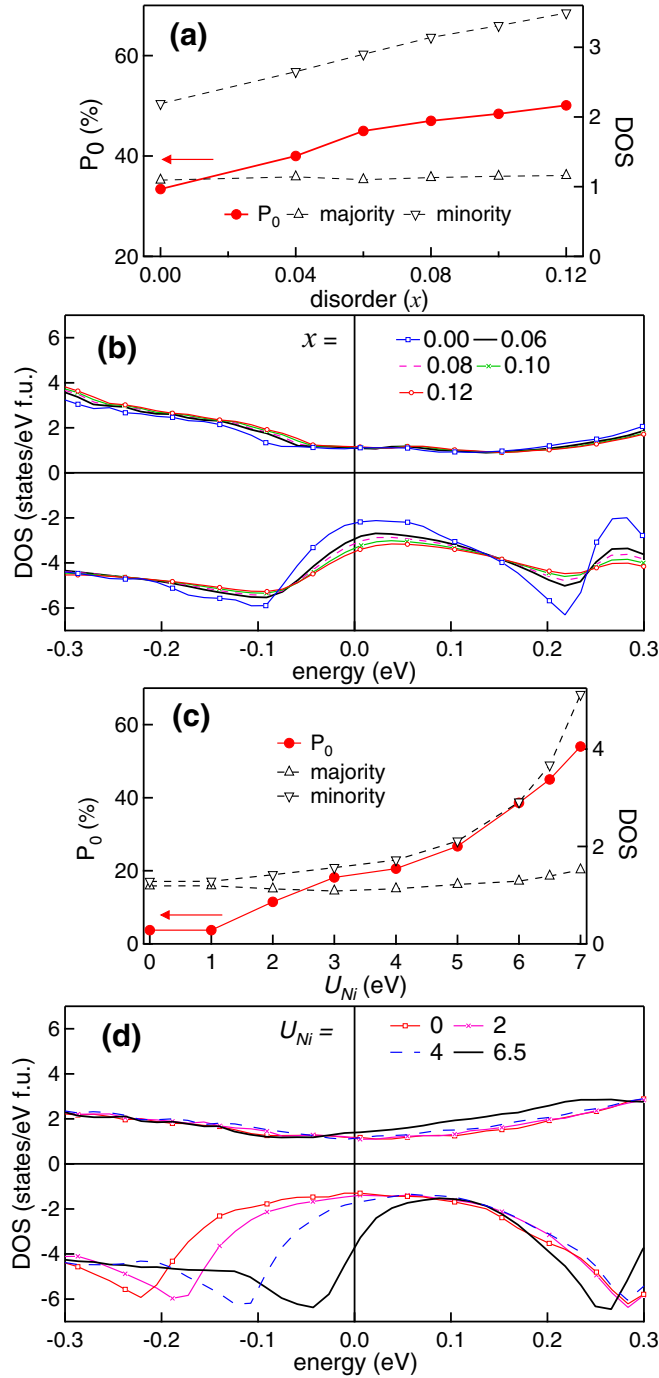


FIG. 8. Spin polarization (P_0), majority $[n_{\uparrow}(E_F)]$, and minority $[n_{\downarrow}(E_F)]$ spin total DOS at E_F (a) as a function of disorder (x) with $U_{Ni} = U_{Mn} = U_{Ce} = 0$ and (c) as a function of U_{Ni} , where $U_{Mn} = 4.5$ eV, $U_{Ce} = 7$ eV and $x = 0$. Majority and minority spin total DOS around E_F corresponding to (a) and (c) as a function of (b) x and (d) U_{Ni} , respectively.

to -0.05 eV [Fig. 8(d)]. Clearly, the total DOS is dominated by Ni 3d, black ticks in Fig. 10 show how the minority spin Ni 3d PDOS peak shifts with U_{Ni} . In contrast, the majority spin total DOS is structureless and $n_{\uparrow}(E_F)$ remains almost unchanged [Figs. 8(c) and 8(d)]. The partial contributions to

TABLE I. The total spin polarization (P_0 , also see Fig. 8) and the partial contributions to P_0 from the Ni 3d (P_{0Ni3d}), Mn 3d (P_{0Mn3d}), and Ce 4f (P_{0Ce4f}) PDOS, as functions of Mn-Ni antisite disorder (x) and Ni 3d electron-electron correlation (U_{Ni}). P_0 is calculated using the following formula: $P_0 = |[n_{\uparrow}(E_F) - n_{\downarrow}(E_F)] / [n_{\uparrow}(E_F) + n_{\downarrow}(E_F)]|$, where $n_{\uparrow}(E_F)$ is the majority spin total DOS at E_F and $n_{\downarrow}(E_F)$ is the minority spin total DOS at E_F . The partial contributions to P_0 from an Xnl PDOS (P_{0Xnl}) where $X = Ni, Mn$ or Ce ; $n = 3 - 6$; $l = s, p, d, \text{ or } f$ is given by $P_{0Xnl} = |[n_{\uparrow Xnl}(E_F) - n_{\downarrow Xnl}(E_F)] / [n_{\uparrow Xnl}(E_F) + n_{\downarrow Xnl}(E_F)]|$, where $n_{\uparrow Xnl}(E_F)$ is the majority spin Xnl PDOS at E_F and $n_{\downarrow Xnl}(E_F)$ is the minority spin Xnl PDOS at E_F . Note that $P_0 = \sum_{X,n,l} P_{0Xnl}$, when all possible X, n, l are considered.

x	Mn-Ni antisite disorder				Ni 3d electron-electron correlation				
	P_0 (%)	P_{0Ni3d} (%)	P_{0Mn3d} (%)	P_{0Ce4f} (%)	U_{Ni}	P_0 (%)	P_{0Ni3d} (%)	P_{0Mn3d} (%)	P_{0Ce4f} (%)
0	33.4	13.4	10.4	7	3	18.2	4.9	3.3	5.8
0.04	40	18.6	9.2	7.5	4	20.6	9.1	3.2	5.2
0.06	45	21.4	9.1	8.4	5	26.7	15	3	5.2
0.08	47	23.1	9.2	9.3	6	38.6	25.3	2.7	5.6
0.10	48.4	24.3	8.8	8.9	6.5	45	32.2	2.4	5.4
0.12	50.1	25.3	8.8	9	7	54	42	2	5.2

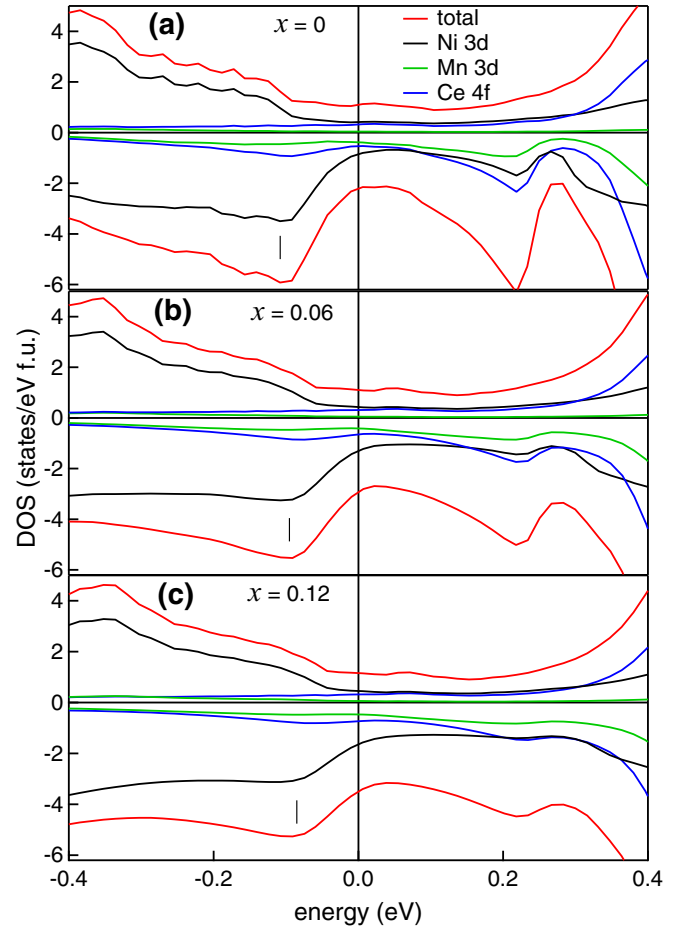


FIG. 9. Spin-polarized total, Ni 3d, Mn 3d, and Ce 4f PDOS in a small range around E_F , as a function of antisite disorder (a) $x = 0$, (b) $x = 0.06$, and (c) $x = 0.12$.

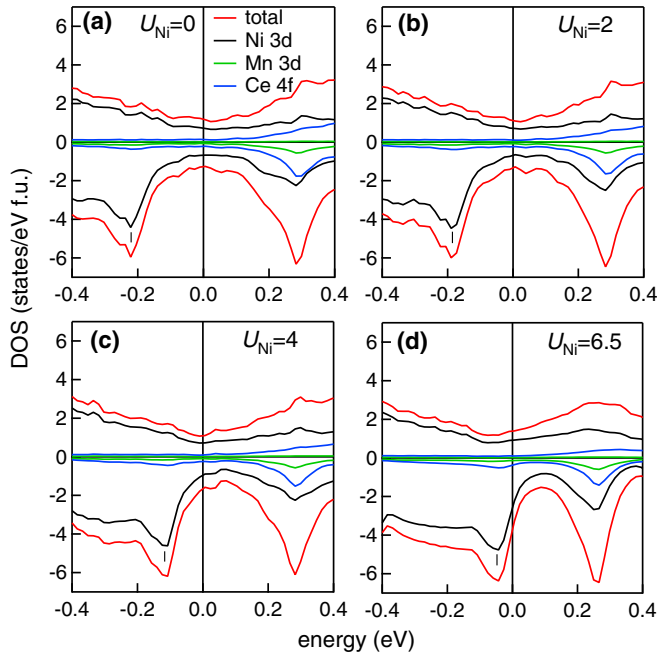


FIG. 10. Spin-polarized total, Ni 3d, Mn 3d, and Ce 4f PDOS in a small range around E_F , as a function of U_{Ni} with $U_{Mn} = 4.5$ eV and $U_{Ce} = 7$ eV for $U_{Ni} =$ (a) 0 eV, (b) 2 eV, (c) 4 eV, and (d) 6.5 eV. The black ticks show the position of Ni 3d minority spin peak that shifts toward E_F with U_{Ni} .

P_0 for different U_{Ni} clearly show that the increase in P_0 is entirely due to P_{0Ni3d} (Table I).

Due to disorder, the Ni 3d minority spin peak will broaden and also possibly shift by a small amount toward E_F and thus significantly increase $n_{\downarrow}(E_F)$ because of its proximity to E_F , e.g., at -0.05 eV for $U(4.5,6.5,7)$. On the other hand, $n_{\uparrow}(E_F)$ would remain unchanged due to the nearly flat nature of the majority spin total DOS. Thus, disorder would further increase P_0 , and assuming that its effect is independent of U , we estimate P_0 for $U(4.5,6.5,7)$ to increase from 45% to $>55\%$ ($>60\%$) for $x = 0.06$ (0.12). This is in good agreement with the experimental value of 66%, given the fact that the measurements were performed in the diffusive limit [4] and here we calculate the static spin polarization.

We have also studied how U_{Mn} and U_{Ce} affect P_0 and find that both have a detrimental effect: In Fig. 11(a), $P_0(U_{Mn},0,0)$ shows a decrease from 33.4% to 11.4% with U_{Mn} varying from 0 to 7 eV. In comparison, the effect of U_{Ce} is milder with $P_0(0,0,U_{Ce})$ decreasing from 33.4% to 28%. If U_{Mn} and U_{Ce} are set to 0, P_0 increases to a large value of 66% for $U_{Ni} = 7$ eV, i.e., for $U(0,7,0)$ [black filled squares in Fig. 11(a)]. On the other hand, a comparison of $P_0(U_{Ni})$ for $(0,U_{Ni},0)$, $(5,U_{Ni},0)$, $(4.5,U_{Ni},7)$ shows that the extent of increase of P_0 is clearly arrested when U_{Mn} and U_{Ce} are nonzero. These results refute an earlier counterintuitive report[9], which concluded that U_{Mn} increases P_0 , while neither U_{Ni} nor U_{Ce} have any influence on P_0 (see the Discussion SD1 and Fig. S2) [22].

The calculated magnetic moments show that the total moment of $CeMnNi_4$ is quite large, e.g., $5.43 \mu_B$ for $U(4.5,6.5,7)$, the main contribution coming from the Mn spin moment ($4.31 \mu_B$). Figure 11(b) shows that both the total moment as well as the Ni spin moment increase with U_{Ni} ,

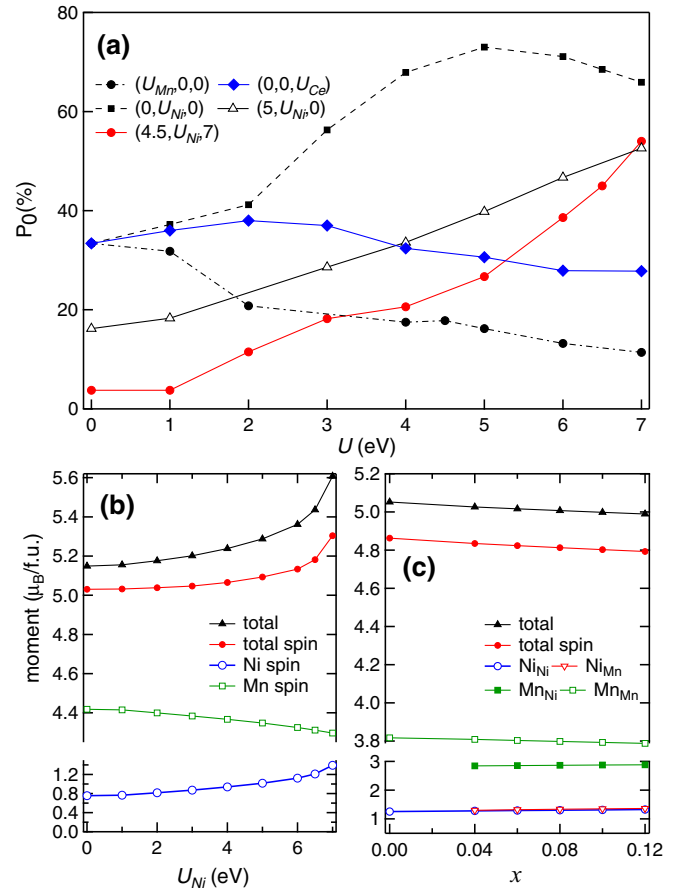


FIG. 11. (a) Spin polarization P_0 as a function of electron-electron correlation U for Ni 3d (U_{Ni}), Mn 3d (U_{Mn}) and Ce 4f electrons (U_{Ce}). P_0 is plotted as a function of U shown as a triplet (U_{Mn}, U_{Ni}, U_{Ce}), where the fixed U values in the triplet are indicated by numbers in eV. For example, $(5, U_{Ni}, 0)$ means U_{Ni} varies from 0 to 7 eV with U_{Mn} and U_{Ce} fixed at 5 eV and 0 eV, respectively. The total (spin plus orbital) moment, the total spin only moment of $CeMnNi_4$, and the local spin magnetic moments of Mn and Ni are plotted (b) as a function of U_{Ni} with $U_{Mn} = 4.5$ eV, $U_{Ce} = 7$ eV and $x = 0$; and (c) as a function of disorder (x). In all cases, the Ce atom possess a small opposite moment of $-0.2 \mu_B$.

e.g., for $U(4.5,0,7)$ the total moment (Ni spin moment) is 5.15 (0.19) μ_B , whereas for $U(4.5,6.5,7)$ it is 5.43 (0.3) μ_B . The increase in the Ni spin moment is because of the shift of the Ni 3d minority spin states toward E_F [Fig. 10(d)], resulting in a decrease of the integrated occupied minority spin PDOS, while the majority spin PDOS remains largely unchanged. It may be noted that the total moment of $5.43 \mu_B$ for $U(4.5,6.5,7)$ is somewhat overestimated compared to the experimental value of $4.95 \mu_B$ from magnetization measurement at 5 K[4].

Interestingly, we find that the total magnetic moment decreases with increasing disorder [Fig. 11(c)]. This can be ascribed to the difference of the Mn_{Ni} (Mn atom in Ni position) and Mn_{Mn} (Mn atom in Mn position) 3d spin-polarized PDOS, the latter having considerably reduced exchange splitting (Fig. 3). This difference is related to the change in hybridization due to different nearest-neighbor configurations

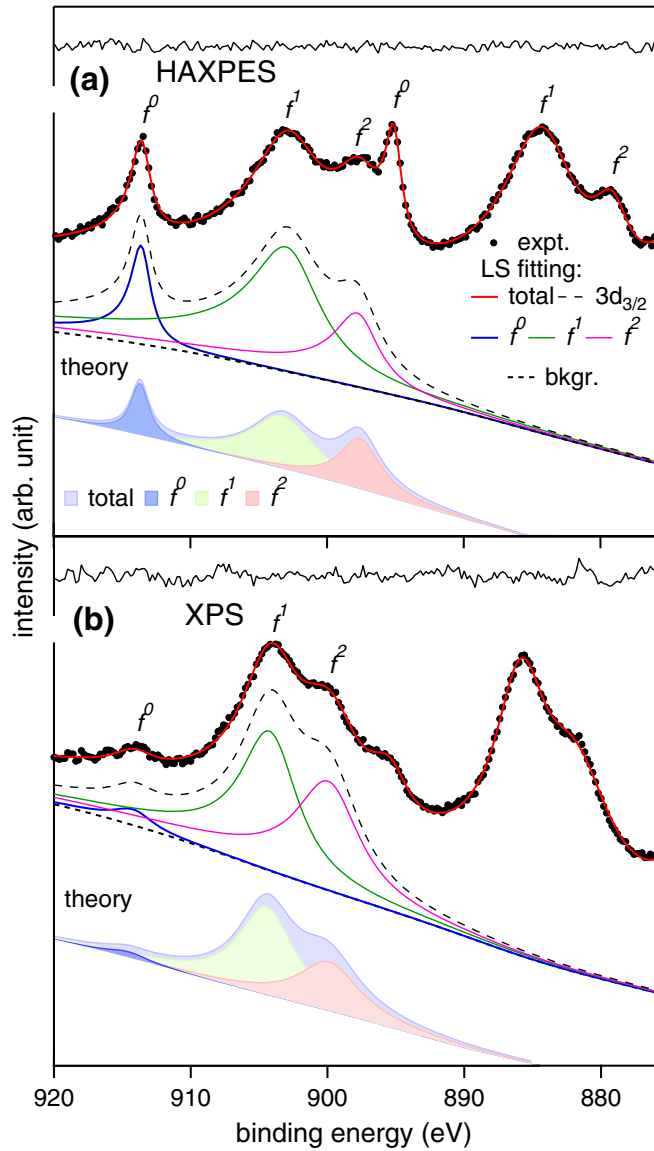


FIG. 12. Ce $3d$ core-level spectra (black dots) recorded with (a) 8 keV (HAXPES) and (b) 1.48 keV (XPS) photon energies. The spectra have been fitted (red line) using a least-squares (LS) error minimization routine and the f^n satellite components for Ce $3d_{3/2}$ are shown. The calculated Ce $3d_{3/2}$ spectra using IW theory along with the f^n satellites are shown at the bottom and the residuals of fitting (black line) are shown at the top of each panel.

(Fig. 1). The local moment of Mn_{Ni} is thus substantially smaller ($2.8 \mu_B$) compared to Mn_{Mn} ($3.8 \mu_B$). Although the local moments hardly vary, the proportion of Mn_{Ni} increases with x , resulting in a decrease of the total moment. Thus, it can be argued that the overestimation of the total moment by theory with $U(4.5, 6.5, 7)$ mentioned above could be somewhat compensated by its decrease caused by antisite disorder.

C. Surface valence transition

An interesting outcome of our work that emerges from the study of the Ce $3d$ core-level spectra is the demonstration

of a valence state transition, i.e., a change of the valency of Ce between the bulk and the surface. Valence state transition could significantly alter the surface electronic structure compared to the bulk. It was first reported in Sm metal [24], where the top atomic layer had a large divalent component [24]. Subsequently, valence transition has also been observed in binary Ce intermetallic compounds, where the surface has larger $4f$ occupancy [25].

The Ce $3d$ core-level spectrum in Fig. 12 displays two sets of triplet peaks corresponding to the s.o. split components. The most intense among the triplet peaks is the f^1 satellite associated with a poorly screened $3d^9 4f^1$ final state occurring at 902.8 eV and 884.4 eV binding energies. The two additional satellite peaks that occur at relatively higher and lower binding energies are referred to as f^0 and f^2 , respectively. The well-screened f^2 satellite has an extra screening electron with $3d^9 4f^2$ final state, while the f^0 satellite is related to $3d^9 4f^0$ final state [26,27]. Notable in Fig. 12 is the large f^0 intensity in HAXPES, which decreases drastically in soft x-ray PES (XPS). To extract quantitative information, the Ce $3d$ core-level spectra were fitted using a least-squares error minimization routine as discussed in the Methods section.

From the least-squares fitting, we find that the normalized intensity of f^0 ($I_n(f^0)$) is 0.15 for HAXPES, where $I_n(f^0) = I(f^0) / \sum_{n=0}^2 I(f^n)$ (Table II). Such large intensity of f^0 having almost similar height as f^1 is unusual and has not been observed in other Ce-based intermetallic compounds [28,29]. In contrast, $I_n(f^0)$ is an order of magnitude less (0.04) in XPS. This could be related to the bulk sensitivity of HAXPES with mean free path (λ) of 91 Å for Ce $3d$ electrons with $h\nu = 8$ keV, while XPS is surface sensitive with $\lambda = 13$ Å [30] with $h\nu = 1.48$ keV. To understand the differences between the above-discussed bulk and surface Ce $3d$ spectra, we turn to a simplified version of the Anderson single-impurity model [31] proposed by Imer and Wuilloud (IW), where the extended valence states are considered as a band of infinitely narrow width [11]. The Ce $3d$ spectrum is calculated as a function of the energy of the unhybridized $4f$ state relative to E_F (ϵ_f), Coulomb repulsion between $4f$ electrons at the same site (U_{ff}), Coulomb attraction between $4f$ electron and the final-state core hole (U_{fc}), and hybridization between the $4f$ states and the conduction band (Δ).

The above-mentioned parameters are varied such that the f^n satellites of the calculated Ce $3d_{3/2}$ spectrum have similar intensities (I_n) and energy separations between f^0 and f^n (δ_{0n}), as obtained from the fitting of the experimental spectra. For example, besides the large change in $I_n(f^0)$, the binding energies of the f^n satellites are lower in HAXPES, resulting in different δ_{0n} as shown in Table II. This is not due to recoil effect that is generally observed in light materials, which shifts the spectrum to higher binding energy [1]. The recoil effect, if present causes a uniform shift of the peaks to higher binding energies that increases with the kinetic energy of the electrons, which in turn depends on the photon energy used. We confirm the absence of recoil effect for CeMnNi₄ from the Ni $2p$ spectra taken with different photon energies, where any shift of the peaks for different photon energies is absent (Fig. 13). A satellite feature (black ticks) is observed at 859.4 eV, i.e., about 6.6 eV higher binding energy from the $2p_{3/2}$ main peak

TABLE II. The parameters for Ce $3d_{3/2}$ such as normalized intensity $I_n(f^n)$, binding energy (E_B), energy separation δ_{0n} between f^n satellites obtained from least-squares fitting compared with those obtained from IW theory. All the values are in eV and $U_{ff} = 7$ eV in both cases. The error in $I_n(f^0)$ is significantly smaller because the f^0 satellite is well separated in energy from all the other components.

$h\nu$ (keV)	PES experiment				IW theory				
	f^n	I_n	$E_B \pm 0.2$	$\delta_{0n} \pm 0.4$	ϵ_f	Δ	U_{fc}	I_n	δ_{0n}
8	f^0	0.15 ± 0.01	913.5	0				0.15	0
	f^1	0.6 ± 0.1	902.8	10.7	-1.0	1.5	10	0.53	10.5
	f^2	0.25 ± 0.1	897.8	15.7				0.32	16.1
1.48	f^0	0.04 ± 0.01	914.3	0				0.04	0
	f^1	0.5 ± 0.1	904.1	10.2	-2.5	1.1	8	0.62	10.1
	f^2	0.45 ± 0.1	899.9	14.4				0.34	14.7

for all photon energies. This can be assigned to the well known 6 eV satellite of Ni metal that arises due to electron-electron correlation in the narrow Ni $3d$ band [32]. The presence of this satellite feature further confirms the importance of electron-electron correlation in the Ni $3d$ states of CeMnNi₄.

To simulate the HAXPES spectra using IW theory, we note that $I_n(f^0)$ increases sensitively with ϵ_f , and so this parameter is varied keeping the others fixed at the values suggested for Ce compounds ($\Delta = 1.5$ eV, $U_{ff} = 7$ eV, $U_{fc} = 10$ eV) [11]. For $\epsilon_f = -1$ eV, we find $I_n(f^0) = 0.15$ in excellent agreement with experiment; and the other quantities such as δ_{0n} , $I_n(f^1)$ and $I_n(f^2)$ are also in good agreement (Table II). The calculated spectrum obtained with $\epsilon_f = -1$ eV, $\Delta = 1.5$ eV, $U_{ff} = 7$ eV, $U_{fc} = 10$ eV is shown at the bottom of Fig. 12(a), where the f^n satellites have been broadened by their respective widths obtained from the fitting. The f occupancy in the ground state (n_f) turns out to be 0.8, indicating a mixed valent state with 20% Ce in f^0 (Ce^{4+}) while 80% in f^1 (Ce^{3+}) configuration.

To simulate the Ce $3d$ XPS spectrum, we decrease ϵ_f to -2.5 eV from the HAXPES value of -1 eV and obtain

$I_n(f^0) = 0.04$. But concomitantly, both δ_{01} ($=12.1$ eV) and δ_{02} ($=18.9$ eV) become larger than experimental values of 10.2 eV and 14.4 eV, respectively (Table II). To decrease δ_{0n} , both Δ and U_{fc} need to be decreased, and thus, we obtain a good agreement with experiment for $\epsilon_f = -2.5$ eV, $\Delta = 1.1$ eV, $U_{fc} = 8$ eV, and $U_{ff} = 7$ eV [bottom of Fig. 12(b)]. Due to the decrease of ϵ_f , n_f increases to 0.98, and thus, in contrast to bulk, at the surface Ce has predominantly $3d^9 4f^1$ (Ce^{3+}) ground state. Thus, in the bulk, since ϵ_f ($=-1$ eV) is closer to E_F and Δ is larger, the Ce $4f$ electron transfers to the valence states comprising of primarily Ni $3d$ states, making CeMnNi₄ a mixed valent system with $4f$ occupancy of $n_f = 0.8$. However, at the surface, the reduced hybridization between the Ce $4f$ and unsaturated $3d$ states results in a lowering of the Ce $4f$ states further below E_F . This increases the occupancy of the Ce $4f$ level ($n_f = 0.98$) and results in the surface valence transition. Decrease in U_{fc} from about 10 eV to 8 eV at the surface is also a manifestation of this transition possibly caused by the more efficient screening of the core hole due to increased n_f . Finally, although the valence transition manifests clearly in Ce $3d$ XPS spectrum, it does not, however, result in the appearance of any Ce $4f$ peak in the XPS VB because of largely diminished Ce $4f$ PDOS compared to Ni $3d$ PDOS in the occupied region as well as lower photoemission cross section of Ce $4f$ compared to Ni $3d$ (see Discussion SD2 and Fig. S3) [22].

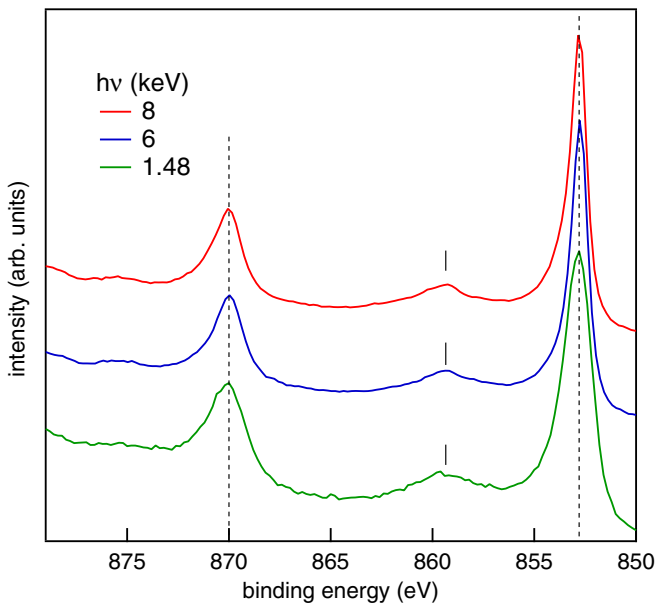


FIG. 13. Ni $2p$ core-level spectra of CeMnNi₄ using 8, 6, and 1.48 keV photon energies, normalized to same height at the Ni $2p_{3/2}$ peak and staggered along the vertical axis for clarity of presentation.

III. CONCLUSION

In conclusion, we settle the long-standing debate about the electronic structure of CeMnNi₄. We establish the importance of both antisite disorder and electron-electron correlation in explaining its intriguing properties. Our work fundamentally alters the general notion that antisite disorder is detrimental for spin polarization. We hope it will motivate further experimental work on CeMnNi₄ and related materials, mainly because disorder could be controlled and P_0 further enhanced. We find that the total magnetic moment exhibits contrasting behavior, it decreases with x , but increases with U_{Ni} . A valence state transition that originates due to the weakened hybridization on the surface is demonstrated. Our study highlights the power of HAXPES in combination with DFT for clarifying the electronic structure and properties of multiply correlated materials with inherent antisite disorder.

ACKNOWLEDGMENTS

The HAXPES experiments were carried out at PETRA III of Deutsches Elektronen-Synchrotron, a member of Helmholtz-Gemeinschaft Deutscher Forschungszentren. Financial support by the Department of Science and Technology, Government of India within the framework of India@DESY collaboration is gratefully acknowledged. We would like to thank W. Drube and C. Narayana for support and encouragement. S.W.D. gratefully acknowledges the financial

support from CEDAMNF Project No. CZ.02.1.01/0.0/0.0/15-003/0000358. A. Chakrabarti thanks P. A. Naik and A. Banerjee for support and encouragement and the Computer Centre of RRCAT, Indore for providing the computational facility for a part of the work. A. Chainani thanks the Ministry of Science and Technology of the Republic of China, Taiwan for financially supporting this research under Contract No. MOST 106-2112-M-213-001-MY2.

P.S. and S.W.D. contributed equally to the work.

- [1] C. S. Fadley, *J. Electron Spectrosc. Relat. Phenom.* **178–179**, 2 (2010); K. Kobayashi, *Nucl. Instrum. Methods Phys. Res., Sect. A* **601**, 32 (2009).
- [2] *Hard X-ray Photoelectron Spectroscopy*, edited by J. C. Woicik, Springer Series in Surface Sciences (Springer International Publishing, Switzerland, 2016), Vol. 59.
- [3] A. X. Gray, C. Papp, S. Ueda, B. Balke, Y. Yamashita, L. Plucinski, J. Minár, J. Braun, E. R. Ylvisaker, C. M. Schneider, W. E. Pickett, H. Ebert, K. Kobayashi, and C. S. Fadley, *Nat. Mater.* **10**, 759 (2011); **11**, 958 (2012); *Phys. Rev. Lett.* **108**, 257208 (2012); J. Nayak, M. Maniraj, A. Rai, S. Singh, P. Rajput, A. Gloskovskii, J. Zegenhagen, D. L. Schlagel, T. A. Lograsso, K. Horn, and S. R. Barman, *ibid.* **109**, 216403 (2012); T. Ohtsuki, A. Chainani, R. Eguchi, M. Matsunami, Y. Takata, M. Taguchi, Y. Nishino, K. Tamasaku, M. Yabashi, T. Ishikawa, M. Oura, Y. Senba, H. Ohashi, and S. Shin, *ibid.* **106**, 047602 (2011); M. Sing, G. Berner, K. Goss, A. Müller, A. Ruff, A. Wetscherek, S. Thiel, J. Mannhart, S. A. Pauli, C. W. Schneider, P. R. Willmott, M. Gorgoi, F. Schäfers, and R. Claessen, *ibid.* **102**, 176805 (2009).
- [4] S. Singh, G. Sheet, P. Raychaudhuri, and S. K. Dhar, *Appl. Phys. Lett.* **88**, 022506 (2006).
- [5] H. Ebert, D. Ködderitzsch, J. Minár, *Rep. Prog. Phys.* **74**, 096501 (2011).
- [6] I. Dhiman, A. Das, S. K. Dhar, P. Raychaudhuri, S. Singh, and P. Manfrinetti, *Solid State Commun.* **141**, 160 (2007).
- [7] I. Mazin, *Phys. Rev. B* **73**, 012415 (2006); E. N. Voloshina, Y. S. Dedkov, M. Richter, and P. Zahn, *ibid.* **73**, 144412 (2006).
- [8] D. Lahiri, S. Khalid, P. Modak, P. Raychaudhuri, S. K. Dhar, and S. M. Sharma, *Phys. Rev. B* **82**, 134424 (2010).
- [9] M. S. Bahramy, P. Murugan, G. P. Das, and Y. Kawazoe, *Phys. Rev. B* **81**, 165114 (2010).
- [10] $P_0 = |[n_{\uparrow}(E_F) - n_{\downarrow}(E_F)]/[n_{\uparrow}(E_F) + n_{\downarrow}(E_F)]|$.
- [11] J.-M. Imer and E. Wuilloud, *Z. Phys. B* **66**, 153 (1987).
- [12] A. Gloskovskii, G. Stryganyuk, G. H. Fecher, C. Felser, S. Thiess, H. Schulz-Ritter, W. Drube, G. Berner, M. Sing, R. Claessen, and M. Yamamoto, *J. Electron Spectrosc. Relat. Phenom.* **185**, 47 (2012).
- [13] J. P. Perdew, K. Burke, and M. Ernzerhof, *Phys. Rev. Lett.* **77**, 3865 (1996).
- [14] H. Ebert, A. Perlov, and S. Mankovsky, *Solid State Commun.* **127**, 443 (2003).
- [15] P. Lloyd, *Proc. Phys. Soc.* **90**, 207 (1967); P. Lloyd and P. V. Smith, *Adv. Phys.* **21**, 69 (1972); R. Zeller, *J. Phys.: Condens. Matter* **20**, 035220 (2008).
- [16] J. J. Yeh and I. Lindau, *At. Data Nucl. Data Tables* **32**, 1 (1985); M. B. Trzaskovskaya and V. G. Yarzhemsky, *ibid.* **119**, 99 (2018).
- [17] G. Panaccione, G. Cautero, M. Cautero, A. Fondacaro, M. Grioni, P. Lacovig, G. Monaco, F. Offi, G. Paolicelli, M. Sacchi, N. Stojić, G. Stefani, R. Tommasini, and P. Torelli, *J. Phys.: Condens. Matter* **17**, 2671 (2005).
- [18] A. Fujimori and F. Minami, *Phys. Rev. B* **30**, 957 (1984); S. R. Barman and D. D. Sarma, *ibid.* **51**, 4007 (1995).
- [19] D. A. Shirley, *Phys. Rev. B* **5**, 4709 (1972).
- [20] C. Zborowski, O. Renault, A. Torres, Y. Yamashita, G. Grenet, and S. Tougaard, *Appl. Surf. Sci.* **432**, 60 (2018); S. Tougaard, *Surf. Sci.* **216**, 343 (1989).
- [21] S. Doniach and M. Šunjić, *J. Phys. C* **3**, 287 (1970).
- [22] See Supplemental Material at <http://link.aps.org/supplemental/10.1103/PhysRevB.99.035102> for Figs. S1–S3 and Discussions SD1–SD2.
- [23] K. Özdoğan, E. Şaşıoğlu, B. Aktaş, I. Galanakis, *Phys. Rev. B* **74**, 172412 (2006); Y. Miura, K. Nagao, and M. Shirai, *ibid.* **69**, 144413 (2004).
- [24] G. K. Wertheim and G. Crecelius, *Phys. Rev. Lett.* **40**, 813 (1978); B. Johansson, *Phys. Rev. B* **19**, 6615 (1979).
- [25] C. Laubschat, E. Weschke, C. Holtz, M. Domke, O. Strebler, and G. Kaindl, *Phys. Rev. Lett.* **65**, 1639 (1990).
- [26] F. U. Hillebrecht and J. C. Fuggle, *Phys. Rev. B* **25**, 3550 (1982).
- [27] J. C. Fuggle, F. U. Hillebrecht, Z. Zolnierrek, R. Lässer, Ch. Freiburg, O. Gunnarsson, and K. Schönhammer, *Phys. Rev. B* **27**, 7330 (1983).
- [28] M. Yano, A. Sekiyama, H. Fujiwara, Y. Amano, S. Imada, T. Muro, M. Yabashi, K. Tamasaku, A. Higashiya, T. Ishikawa, Ōnuki, and S. Suga, *Phys. Rev. B* **77**, 035118 (2008).
- [29] M. Sundermann, F. Strigari, T. Willers, J. Weinen, Y. F. Liao, K.-D. Tsuei, N. Hiraoka, H. Ishii, H. Yamaoka, J. Mizuki, Y. Zekko, E. D. Bauer, J. L. Sarrao, J. D. Thompson, P. Lejay, Y. Muro, K. Yutani, T. Takabatake, A. Tanaka, N. Hollmann, L. H. Tjeng, and A. Severing, *J. Electron Spectrosc. Relat. Phenom.* **209**, 1 (2016).
- [30] S. Tanuma, C. J. Powell, and D. R. Penn, *Surf. Interface Anal.* **43**, 689 (2011); C. J. Powell, A. Jablonski, I. S. Tilinin, S. Tanuma, and D. R. Penn, *J. Electron Spectrosc. Relat. Phenom.* **98–99**, 1 (1999).
- [31] O. Gunnarsson and K. Schönhammer, *Phys. Rev. B* **28**, 4315 (1983).
- [32] S. Hüfner and G. Wertheim, *Phys. Lett.* **51A**, 299 (1975).